

# The Anatomy of Star Formation in NGC 300

G. Helou,<sup>1</sup> H. Roussel,<sup>2</sup>

P. Appleton,<sup>1</sup> D. Frayer,<sup>1</sup> S. Stolovy,<sup>1</sup> L. Storrie-Lombardi,<sup>1</sup> R. Hurt,<sup>1</sup> P. Lowrance,<sup>1</sup>  
 D. Makovoz,<sup>1</sup> F. Masci,<sup>1</sup> J. Surace,<sup>1</sup> K.D. Gordon,<sup>3</sup> A. Alonso-Herrero,<sup>3</sup> C.W. Engelbracht,<sup>3</sup>  
 K. Misselt,<sup>3</sup> G. Rieke,<sup>3</sup> M. Rieke,<sup>3</sup> S.P. Willner,<sup>4</sup> M. Pahre,<sup>4</sup> M.L.N. Ashby,<sup>4</sup>  
 G.G. Fazio,<sup>4</sup> H.A. Smith<sup>4</sup>

## ABSTRACT

The *Spitzer Space Telescope* was used to study the mid-infrared to far-infrared properties of NGC 300, and to compare dust emission to H $\alpha$  to elucidate the heating of the ISM and the star formation cycle at scales  $< 100$  pc. The new data allow us to discern clear differences in the spatial distribution of  $8\ \mu\text{m}$  dust emission with respect to  $24\ \mu\text{m}$  dust and to H II regions traced by the H $\alpha$  light. The  $8\ \mu\text{m}$  emission highlights the rims of H II regions, and the  $24\ \mu\text{m}$  emission is more strongly peaked in star forming regions than  $8\ \mu\text{m}$ . We confirm the existence and approximate amplitude of interstellar dust emission at  $4.5\ \mu\text{m}$ , detected statistically in Infrared Space Observatory (ISO) data, and conclude it arises in star forming regions. When averaging over regions larger than  $\sim 1$  kpc, the ratio of H $\alpha$  to Aromatic Feature emission in NGC 300 is consistent with the values observed in disks of spiral galaxies. The mid-to-far-infrared spectral energy distribution of dust emission is generally consistent with pre-Spitzer models.

*Subject headings:* galaxies: ISM — infrared: galaxies — individual: galaxy (NGC 300)

## 1. Introduction

NGC 300 is a SA(s)d galaxy in the Sculptor Group of galaxies, at a distance of about 2.1 Mpc (Freedman et al. 1992), viewed at an inclination of about  $50^\circ$  (Puche et al. 1990).

---

<sup>1</sup>SIRTF Science Center, California Institute of Technology, M.S. 220-6, Pasadena, CA 91125

<sup>2</sup>California Institute of Technology, M.S. 320-47, Pasadena, CA 91125

<sup>3</sup>Steward Observatory, University of Arizona, Tucson, AZ 85721

<sup>4</sup>Harvard-Smithsonian Center for Astrophysics, 60 Garden St., Cambridge, MA 02138

Its total luminosities in the blue band (3855–4985Å) and in the far-infrared (42.5–122.5 μm, estimated from Spitzer data) are  $\sim 3.3 \times 10^8 L_{\odot \text{ bol}}$  and  $2.2 \times 10^8 L_{\odot \text{ bol}}$  respectively. Its  $L_{\text{FIR}}/L_{\text{B}}$  ratio is thus very close to the average ratio for the blue magnitude-limited sample studied by Thuan & Sauvage (1992). Due to its large angular extent and low surface brightness, no reliable total radio continuum flux measurement exists (only discrete sources are detected). NGC 300 has a striking appearance in the visible and in H $\alpha$  due to several H II regions with nearly circular shapes and various degrees of filling-in (Deharveng et al. 1988; Hoopes et al. 1996; see Figure 1). Its large HI envelope (Puche et al. 1990) extends well beyond the visible image. Pannuti et al. (2000) reported a total of 44 SNR candidates, evidence that the current star formation activity manifested as H II regions has been on-going for tens of millions of years (see also Butler et al. 2004). Because of its proximity, NGC 300 allows the Spitzer Space Telescope (Werner et al. 2004) to compare dust emission to other ISM components and discern the interplay between the ISM and the star formation cycle at scales  $< 100$  pc.

## 2. Observations and Data Reduction

The IRAC (Fazio et al. 2004) observations of NGC 300 are 12-second frames and map the galaxy in approximately half array spacings, yielding a total time per sky position of 48 s. They were reduced with the standard Spitzer Science Center data reduction pipeline (version 9.5). Due to the readout of bright point sources, the signal was reduced (pulled-down) in some columns of the array<sup>1</sup>; a correction measured from the map was applied. Persistent images left by bright sources were found by median-combining all the dithered positions together and identifying any remaining sources. These objects were removed from individual frames. The data were then combined into a mosaic using a cosmic ray rejection and a background matching applied between overlapping fields of view. The relative photometric uncertainty is of the order of 5%, and the absolute uncertainty is 10%; uncertainty tied to the angular sizes of source and measuring aperture contributes up to 15%.

Images of NGC 300 at 24, 70, and 160 μm were obtained with the MIPS Instrument (Rieke et al. 2004) in the scan-map mode. The final mosaics have a total exposure time of approximately 160, 80, and 16 s per point at 24, 70, and 160 μm. The MIPS images were reduced using the MIPS Instrument Team Data Analysis Tool (Gordon et al. 2004) as described by Engelbracht et al. (2004). The uncertainties on the final absolute calibrations are estimated at 10%, 20%, and 20% for the 24, 70, and 160 μm data, respectively. The

---

<sup>1</sup>see the Spitzer Observer’s Manual at <http://ssc.spitzer.caltech.edu/documents/som/>.

70 and 160  $\mu\text{m}$  images exhibit linear streaks along the scan direction which are residual instrumental artifacts due to the time dependent responsivity of the Ge detectors, and affect the photometry in large apertures.

The  $\text{H}\alpha$  (6563 $\text{\AA}$ ) + [N II] (6583 and 6548 $\text{\AA}$ ) map was derived from images posted in NED by Larsen & Richtler (1999). The narrowband image containing  $\text{H}\alpha$  emission and the R-band image were aligned, and rescaled to subtract the stellar continuum, deriving the scaling factor from aperture photometry on 32 bright stars. Residuals from saturated or improperly subtracted stars were masked out, and the final image was regridded and rotated to match the IRAC reference frame.

The Spitzer and  $\text{H}\alpha$ + [N II] images are shown in Figure 1. The images contain three very bright Milky Way stars directly superposed on the disk. We masked them out in IRAC and 24  $\mu\text{m}$  images, as well as additional point sources as described in Section 3.1 below (Figure 4b). Foreground stars will be removed more rigorously in a later paper. Fainter, indistinguishable stars are unlikely to affect significantly the results presented here.

### 3. Physical Content in Mid-Infrared Images

Whereas at  $\lambda \geq 24 \mu\text{m}$  the emission is dominated by interstellar dust, the mid-infrared marks the transition from stellar to interstellar emission. The appearance of the galaxy shifts from resembling the stellar disk in the 3.6  $\mu\text{m}$  image to an ISM-like appearance at 8  $\mu\text{m}$ . We assume conservatively the 3.6  $\mu\text{m}$  emission is all due to stars, and extrapolate this component to longer wavelengths using stellar population modeling from Starburst99 (Leitherer et al. 1999); the stellar Spectral Energy Distribution (SED) longward of 2  $\mu\text{m}$  depends very little on star formation history or metallicity, as illustrated in Figure 2. The decomposition amounts to scaling the 3.6  $\mu\text{m}$  map by 0.596, 0.399, 0.232 and 0.032 respectively for 4.5, 5.8, 8 and 24  $\mu\text{m}$ , and subtracting these from the observed maps pixel by pixel to yield what we will refer to as the "dust maps" shown in Figure 1. Based on this decomposition, the 24  $\mu\text{m}$  map is probably  $\geq 98\%$  interstellar emission globally, and  $\geq 93\%$  interstellar in the inner arcmin, where the stellar contribution is the greatest. The 8  $\mu\text{m}$  map is  $\geq 81\%$  interstellar emission.

This method potentially overestimates the dust component by underestimating the red-der SED of very low mass stars. However the model reproduces adequately the 4.5  $\mu\text{m}$ /3.6  $\mu\text{m}$  color of the nuclear stellar cluster, of the emission averaged in the inner arcmin (Figure 2), and of the diffuse emission outside several disk H II regions.

On the other hand, the method probably underestimates the dust component by assuming that the 3.6  $\mu\text{m}$  map contains only photospheric emission, ignoring evidence that the

hot dust component stretches down to  $\lambda < 3 \mu\text{m}$  (Bernard et al. 1994; Lu et al. 2003; Hunt et al. 2002). From the ISO data in Figure 6 of Lu et al. (2003), this underestimate may reach a factor of up to 2.6, 10–20% and 3–4%, respectively at 4.5, 5.8 and  $8 \mu\text{m}$ . In view of these opposing potential biases, our conservative approach should be reliable qualitatively for NGC 300, in spite of localized departures due to variations in stellar population colors or dust extinction.

### 3.1. Interstellar Dust Emission

In order to constrain the origin of the  $4.5 \mu\text{m}$  non-stellar emission, we identified pixels where the excess is above the  $3\sigma$  significance threshold in the  $4.5 \mu\text{m}$  "dust map", and examined their colors and locations. In scatter plots of these pixel values *vs.*  $\text{H}\alpha$  or *vs.*  $8 \mu\text{m}$  dust emission, a correlation branch is evident in both cases with moderate slopes in  $f_\nu(4.5 \mu\text{m})/f_\nu(8 \mu\text{m})$  and  $f_\nu(4.5 \mu\text{m})/\text{H}\alpha$  (Figure 3), as well as a branch with very steep, almost vertical slopes. The pixels in the latter branch are strongly associated with the  $3.6 \mu\text{m}$  emission, including the brightest foreground star and a large number of point sources spread almost uniformly across the whole map. We use this excess map as a mask to efficiently remove foreground stars, with additional hand masking of residues around very bright stars.

On the other hand, the branches with moderate  $4.5 \mu\text{m}/8 \mu\text{m}$  and  $4.5 \mu\text{m}/\text{H}\alpha$  ratios map into bright star formation regions, as might be expected (Figure 4a). The global ratio  $\nu f_\nu(4.5 \mu\text{m})/\nu f_\nu(8 \mu\text{m})$  for the selected dust emission amounts to  $\sim 4\%$ . However, summing the pixels in star forming regions with large  $4.5 \mu\text{m}$  excess, dust alone accounts for 17% of the total  $4.5 \mu\text{m}$  emission, probably more if dust contribution to the  $3.6 \mu\text{m}$  emission were accounted for. Two uncertainties remain which will be addressed in future papers: Whether redder SEDs of young stars affect significantly the results in star forming regions; and whether the  $4.5 \mu\text{m}$  dust associates more closely with ionized regions or with Photo-Dissociation Regions (PDR).

The dust maps at 5.8 and  $8 \mu\text{m}$  should be dominated by the Aromatic Features in Emission (AFE) proposed by Puget & Léger (1989) to explain IRAS data, and well studied with ISO (Boulanger et al. 1998; Helou et al. 2000; Lu et al. 2003). The value and variability of the ratios between these bands are of considerable interest in constraining the physical state of the emitters (e.g. de Frees et al. 1993). Lu et al. (2003) found the AFE profiles among galaxies constant to within measurement uncertainty of 15 to 25% in the range 5 to  $12 \mu\text{m}$ ; the Spitzer images can extend this finding to much greater accuracy, and could point to variations within disks on a variety of scales.

We find that  $\nu f_\nu(5.8\ \mu\text{m})/\nu f_\nu(8\ \mu\text{m})$  for dust emission alone is constant to within the uncertainties, with a value of  $0.50 \pm 0.09$  ( $3\sigma$ ) over most of the area where surface brightness is above the  $6\sigma$  level in each of the  $5.8\ \mu\text{m}$  and  $8\ \mu\text{m}$  dust maps.

### 3.2. Comparison to $\text{H}\alpha$

Figure 4c shows a comparison between  $\text{H}\alpha$  and  $8\ \mu\text{m}$  maps at a resolution of  $2 \times \text{FWHM} \sim 5.15'' \sim 50\ \text{pc}$ . In the outer disk, several H II regions as well as more complex structures are visible in the  $\text{H}\alpha$  map, with the corresponding  $8\ \mu\text{m}$  profile flatter and sometimes significantly offset from the  $\text{H}\alpha$  peak. In spite of the complex structure, Figure 4c-d clearly shows the  $8\ \mu\text{m}$  emission highlighting the rims of H II regions. The ratio  $8\ \mu\text{m}/\text{H}\alpha$  goes up by a factor five to ten from inside to just outside the H II region. This ratio may increase by another factor of 2–4 in diffuse regions, but this is uncertain because of limited sensitivity and inaccurate continuum subtraction in the  $\text{H}\alpha$  map. While this behavior is not a complete surprise, the Spitzer data are the first to show it so clearly in a nearby galaxy. Boulanger et al. (1990), Sellgren et al. (1990), Giard et al. (1994) and others have reported sharp boundaries to the AFE, with peaks on molecular cloud surfaces outside ionized regions, and related this to a combination of UV excitation and photo-processing of the AFE carriers. Helou et al. (2001) also speculated that AFE arise primarily in PDRs based on physical arguments rather than direct observations. Inside the H II regions, the Aromatics are depressed probably because of destruction by the ionizing UV (Boulanger et al. 1990).

The sharp contrasts near H II regions between  $8\ \mu\text{m}$  and  $\text{H}\alpha$  are only a small-scale property. Summing over scales larger than about 1 kpc, the ratio between the two tracers is constant to about 40%. The global ratio of  $8\ \mu\text{m}$  to unextincted  $\text{H}\alpha$  is roughly 30% smaller than the average measured in disks of spiral galaxies by Roussel et al. (2001a), which had itself a dispersion of 50% among disks. For this comparison, the total  $\text{H}\alpha + [\text{N II}]$  flux from Hoopes et al. (1996) was corrected for an extinction  $A(\text{H}\alpha) = 0.37$  and an  $\text{H}\alpha/(\text{H}\alpha + [\text{N II}])$  ratio of 0.91, averaged from values of individual H II regions in Webster & Smith (1983). The  $8\ \mu\text{m}$  IRAC flux was converted to  $7\ \mu\text{m}$  flux in the ISO filter LW2 assuming the same spectral shape as in the disk of M 83 (Roussel et al. 2001b), which was verified to reproduce accurately the  $5.8\ \mu\text{m}/8\ \mu\text{m}$  dust ratio of NGC 300.

The star formation rate in the disk of NGC 300 is  $0.08\text{--}0.11\ M_\odot\ \text{yr}^{-1}$  from the  $8\ \mu\text{m}$  emission (as calibrated for solar-metallicity spiral disks by Roussel et al. 2001a), and  $\sim 0.14\ M_\odot\ \text{yr}^{-1}$  from  $\text{H}\alpha$  (as calibrated by Kennicutt 1998). The agreement points to  $8\ \mu\text{m}$  under these conditions as a viable proxy for ionizing flux, and therefore for on-going massive star formation rate. Since the association between  $8\ \mu\text{m}$  and  $\text{H}\alpha$  is not at the atomic process

level however, it will be subject to geometric and other effects, and the use of  $8\ \mu\text{m}$  as such a proxy is unlikely to be valid under all conditions.

Figure 4e-f also shows the  $24\ \mu\text{m}$  emission is more peaked than  $8\ \mu\text{m}$  in star forming regions. The spatial resolution is insufficient to distinguish whether PDRs or ionized regions are more closely associated with the  $24\ \mu\text{m}$  peaks. This confirms earlier suggestions based on global SED analysis that  $24\ \mu\text{m}$  traces heating by the youngest and most massive stars in a galaxy (Helou 2000).

#### 4. Mid-IR to Far-IR SED

In order to study the SED at  $\lambda \geq 8\ \mu\text{m}$ , we identified nineteen emission regions in the dust maps, most centered on a local peak (Figure 5l). After smoothing all maps to the resolution of  $160\ \mu\text{m}$ , we measured the emission of each region in a circular aperture  $2.5 \times \text{FWHM}(160\ \mu\text{m}) = 95'' \sim 1\ \text{kpc}$  in diameter. The resulting photometry is plotted in Figure 5 as various color ratios against  $f_\nu(8\ \mu\text{m})/f_\nu(24\ \mu\text{m})$ , and compared to the ratios expected from pre-Spitzer model SEDs of galaxies (Dale & Helou 2002). These are single-parameter models of dust emission integrated over whole galaxies, and incorporate a power-law distribution of dust over heating intensities. The data and model agree in the *trends*, though there are systematic offsets in the values. These offsets are most simply understood as a systematic discrepancy of  $\sim 30\%$  at  $160\ \mu\text{m}$  and  $\sim 15\%$  at  $70\ \mu\text{m}$  between model and measurement, assuming reliable photometry at 8 and  $24\ \mu\text{m}$ . In view of the simplicity of the models, photometric uncertainties (especially non-linearity effects) and source extent, the agreement between model and data is quite satisfactory, and suggests that beyond a certain scale portions of galaxies may approach full galaxies in their behavior.

The  $160\ \mu\text{m}$  and less so the  $70\ \mu\text{m}$  maps display a striking large halo which echoes several features of the HI envelope. It is unclear at this point whether this reflects unusually cold material in the outer disk, or whether the larger  $160\ \mu\text{m}$  beam is simply more sensitive to low surface brightness features.

#### 5. Summary

The Spitzer Space Telescope data allow us more clearly than ever to dissect the interstellar dust emission components in NGC 300 and to relate them to star formation. The  $8\ \mu\text{m}$  AFE highlights the rims of the H II regions defined by  $\text{H}\alpha$ , confirming it is more closely associated with PDRs than with ionized regions. When averaging over regions larger than

$\sim 1$  kpc, the ratio of  $H\alpha$  to AFE emission in NGC 300 is consistent with the disk value observed in other galaxies. This confirms AFE as a convenient massive star formation rate estimator in disks of galaxies. The mid-IR spectral signature of the AFE is invariant as measured by the ratio  $f_\nu(5.8 \mu\text{m})/f_\nu(8 \mu\text{m})$ , which is essentially constant at  $\sim 50$  pc resolution at the  $\sim 20\%$  ( $3\sigma$ ) measurement accuracy over most of the disk of NGC 300. The  $24 \mu\text{m}$  emission is more strongly peaked than  $8 \mu\text{m}$  in star forming regions. Interstellar dust emission at  $4.5 \mu\text{m}$  is confirmed at about the expected amplitude; for the first time, its spatial distribution associates it clearly with star forming regions. The data cannot distinguish between PDRs and H II regions as the primary origin for either  $4.5$  or  $24 \mu\text{m}$  dust emission. The SED models of (Dale & Helou 2002) apply to  $\sim$ kpc-sized portions in the disk to within the current photometry and calibration uncertainties of 20–30%.

The Spitzer Space Telescope is operated by the Jet Propulsion Laboratory, California Institute of Technology, under contract with the National Aeronautics and Space Administration. This research has made use of the NASA/IPAC Extragalactic Database which is operated by JPL/Caltech, under contract with NASA.

## REFERENCES

- Bernard, J.P., Boulanger, F., Désert, F.X., Giard, M., Helou, G., & Puget, J.L. 1994, *A&A*, 291, L5
- Boulanger, F., Boissel, P., Cesarsky, D., & Ryter, C. 1998, *A&A*, 339, 194
- Boulanger, F., Falgarone, E., Puget, J.-L., & Helou, G. 1990, *ApJ*, 346, 136
- Butler, D.J., Martinez-Delgado, D. & Brandner, W. 2004, *AJ*127, 1472
- Dale, D.A., Helou, G., Contursi, A., Silbermann, N., & Kolhatkar, S. 2001, *ApJ*, 549, 215
- Dale, D.A., & Helou, G. 2002, *ApJ*, 159, 576
- de Frees, D.J., Miller, M.D., Talbi, D., et al. 1993, *ApJ*, 408, 530
- Deharveng, L., Caplan, J., Lequeux, J., et al. 1988, *A&AS*, 73, 407
- Engelbracht, C.W. et al. 2004, *ApJS*, this volume
- Fazio, G. et al. 2004, *ApJS*, this volume
- Freedman, W.L., Madore, B.F., Hawley, S.L., et al. 1992, *ApJ*, 396, 80

- Giard, M., Bernard, J. P., Lacombe, F., Normand, P., & Rouan, D. 1994, *A&A*, 291, 239
- Gordon, K.D. et al. 2004, *PASP*, submitted
- Helou, G. 2000, in “Infrared Astronomy: Today and Tomorrow”, ed. F. Casoli, J. Lequeux & F. David (Springer Verlag: Les Ulis) p. 337
- Helou, G., Lu, N.Y., Werner, M.W., Malhotra, S., & Silbermann, N.A. 2000, *ApJ*, 532, L21
- Helou G., Malhotra S., Hollenbach D.J., Dale D.A. & Contursi A. 2001, *ApJ*, 548, L73
- Hoopes, C.G., Walterbos, R.A., & Greenawalt, B.E. 1996, *AJ*, 112, 1429
- Hunt, L.K., Giovanardi, C., & Helou, G. 2002, *A&A*, 394, 873
- Kennicutt, R.C. 1998, *ARA&A*, 36, 189
- Larsen, S.S., & Richtler, T. 1999, *A&A*, 345, 59
- Leitherer, C., Schaerer, D., Goldader, J.D., et al. 1999, *ApJS*, 123, 3
- Lu, N., Helou, G., Werner, M.W., et al. 2003 *ApJ*, 588, 199
- Pannuti, T.G., Duric, N., Lacey, C., et al. 2000, *ApJ*, 544, 780
- Puche, D., & Carignan, C., & Bosma, A. 1990, *AJ*, 100, 1468
- Puget, J.L. & Léger, A. 1989, *ARA&A*, 27, 161
- Rieke, G. H. et al. 2004, *ApJS*, this volume
- Roussel, H., Sauvage, M., Vigroux, L., & Bosma, A. 2001a, *A&A*, 372, 427
- Roussel, H., Vigroux, L., & Bosma, A., et al. 2001b, *A&A*, 369, 473
- Sellgren, K., Tokunaga, A.T., & Nakada, Y. 1990, *ApJ*, 349, 120
- Thuan, T.X., & Sauvage, M. 1992, *A&AS*, 92, 749
- Webster, B.L., & Smith, M.G. 1983, *MNRAS*, 204, 743
- Werner, M. W. et al. 2004, *ApJS*, this volume



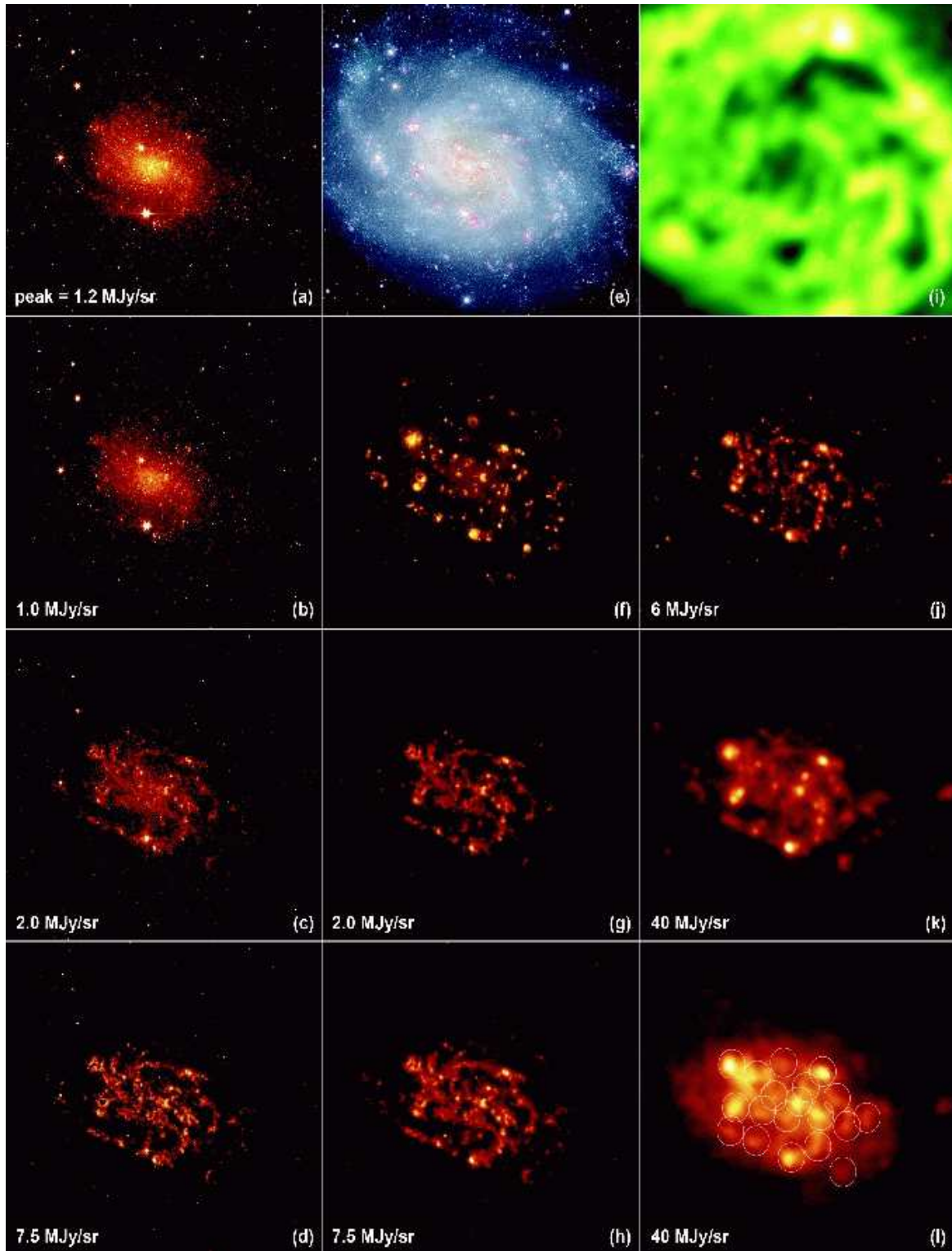


Fig. 1.— Images of NGC 300 obtained with the *Spitzer Space Telescope* and other sources. The left-most column shows observed maps at (a)  $3.6\ \mu\text{m}$ , (b)  $4.5\ \mu\text{m}$ , (c)  $5.8\ \mu\text{m}$ , (d)  $8\ \mu\text{m}$ . The center column shows (e) BVRH $\alpha$  composite image (credit MPG/ESO), where B is coded in blue, V in green, R and H $\alpha$  in red; (f) H $\alpha$  map described in Section 2; (g) dust map at  $5.8\ \mu\text{m}$ ; (h) dust map at  $8\ \mu\text{m}$ . The right-most column shows (i) H I map from Puche et al. (1990); and observed maps at (j)  $24\ \mu\text{m}$ ; (k)  $70\ \mu\text{m}$ ; (l)  $160\ \mu\text{m}$ , with photometric apertures used in Figure 5 superposed. Each frame contains the peak surface brightness in the background-subtracted image; all images are in logarithmic scale, except the  $160\ \mu\text{m}$  image which is linear. North is about  $40^\circ$  clockwise from vertical up, and each frame is approximately  $20'$  on a side.

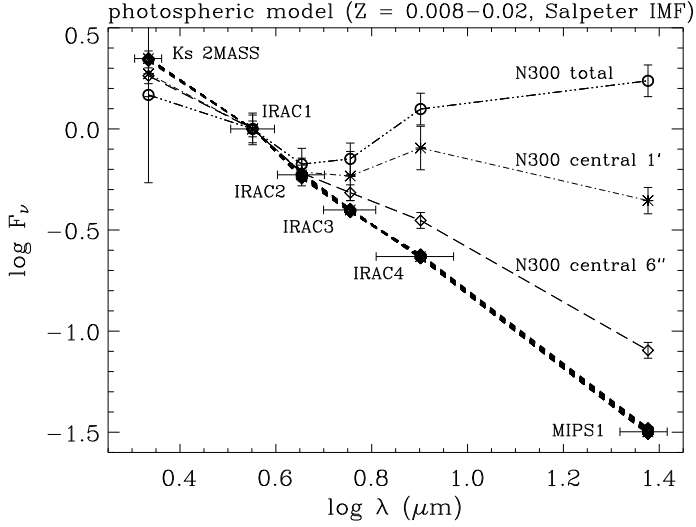


Fig. 2.— SED decomposition: The SEDs of NGC 300 in three different apertures are shown, with all fluxes normalized to  $3.6\ \mu\text{m}$ : the nuclear stellar cluster (clearly contaminated by dust emission judging from morphology in the IRAC maps), the inner arcmin, where dust contribution is relatively small, and the whole galaxy. The thick dashed lines trace model photospheric SEDs from  $2$  to  $24\ \mu\text{m}$ , derived from Starburst99 for a range of star formation histories and two metallicities, and transformed to IRAC filter fluxes. The horizontal error bars represent the filter widths at half maximum transmission. The Ks fluxes are lower limits, because the 2MASS map is not sensitive to the diffuse emission.

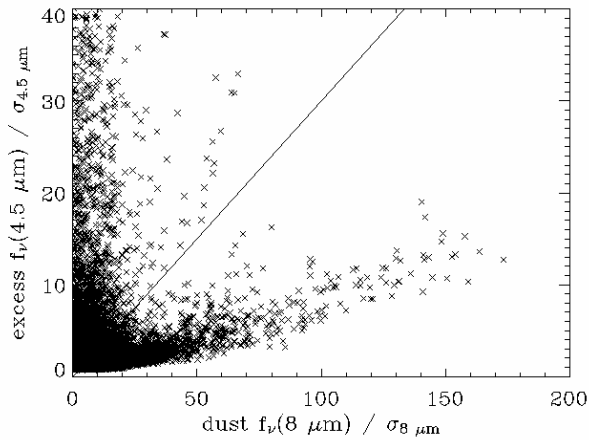


Fig. 3.— Scatter plot of excess  $f_\nu(4.5\ \mu\text{m})$  versus dust-only  $f_\nu(8\ \mu\text{m})$ , normalized by the noise in the original maps. Individual pixels are plotted, after convolution of all maps to a common angular resolution. The correlation branch was isolated by selecting pixels below the solid line (corresponding to Figure 4a). The uncorrelated emission, extending to much higher brightnesses, was cut here for clarity. The scatter plot versus  $\text{H}\alpha$ , not included, shows a similar correlation branch, most pixels of which map into the  $8\ \mu\text{m}$  correlation branch.

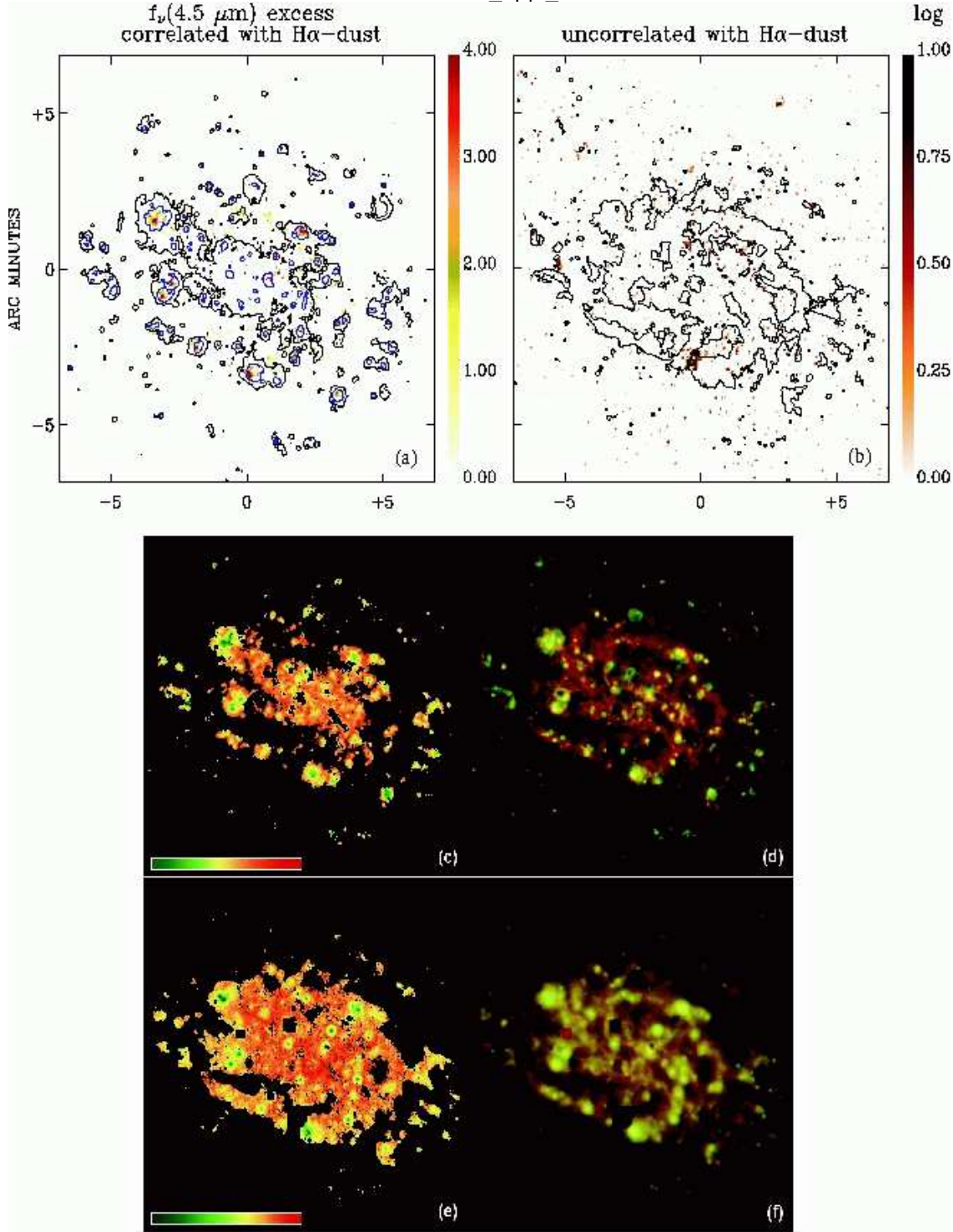


Fig. 4.— **Top:** Distribution of excess 4.5 μm emission,  $f_{\nu}^e(4.5 \mu\text{m})$ , in units of the noise in the initial 4.5 μm map,  $\sigma_{4.5}$ . **(a):** Part of  $f_{\nu}^e(4.5 \mu\text{m})$  which is correlated with 8 μm and Hα (950 pixels  $\in [3; 19] \sigma_{4.5}$ ). **(b):** Part of  $f_{\nu}^e(4.5 \mu\text{m})$  which is not correlated with 8 μm nor Hα, in logarithmic scale (4583 pixels  $\in [3; 8150] \sigma_{4.5}$ ). The contours are Hα isophotes (a) and the  $4\sigma$  isophote of the 8 μm dust map (b). **Bottom:** Comparison of Hα and dust emission: (c)  $\log(f_{\nu}(8 \mu\text{m}) / \text{H}\alpha)$  (95% of pixels span 1.2 dex), showing low ratios inside prominent H II regions; (e)  $\log(f_{\nu}(8 \mu\text{m}) / f_{\nu}(24 \mu\text{m}))$  (95% of pixels span the linear range [0.6; 2.2]), showing again the distinctly low color ratios of H II regions; (d) 8 μm (red) and Hα (green) composite image; (f) 8 μm (red) and 24 μm (green) composite image.

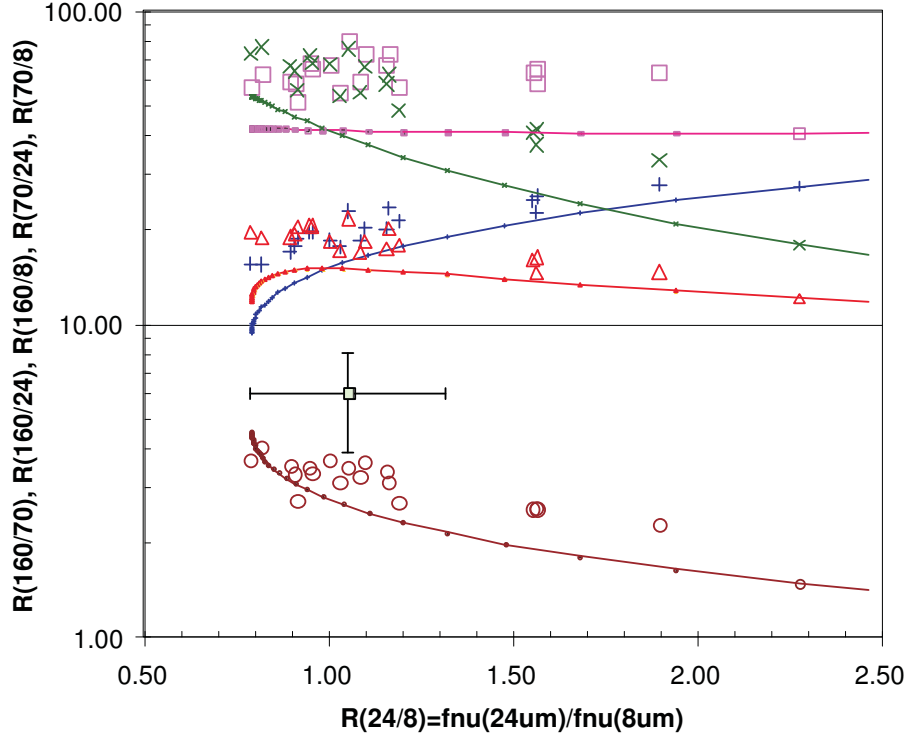


Fig. 5.— Color-color plot for all Spitzer bands at  $\lambda \geq 8 \mu\text{m}$ , for the regions measured with an aperture corresponding to  $\sim 1 \text{ kpc}$  in the plane of NGC 300, with the Dale & Helou (2002) model predictions superposed as curves. Each curve has one symbol at  $x=2.28$  to indicate the corresponding color ratio. We corrected the  $8 \mu\text{m}$  fluxes by a factor of  $\sqrt{0.69}$  since the aperture is intermediate in size between the nominal point-source aperture and infinitely extended scales. The one point with error bars illustrates the uncertainties of 25% on the x-axis and 35% on the y-axis. Squares are for  $160 \mu\text{m}/8 \mu\text{m}$ ; X signs are for  $160 \mu\text{m}/24 \mu\text{m}$ ; plus signs are for  $70 \mu\text{m}/8 \mu\text{m}$ ; triangles are for  $70 \mu\text{m}/24 \mu\text{m}$ ; and circles are for  $160 \mu\text{m}/70 \mu\text{m}$ . The systematic offset at the longer wavelength bands is discussed in the text.